



An ecophysiological explanation for manganese enrichment in rock varnish

Usha F. Lingappa^{a,1}, Chris M. Yeager^b, Ajay Sharma^c, Nina L. Lanza^b, Demosthenes P. Morales^b, Gary Xie^b, Ashley D. Atencio^b, Grayson L. Chadwick^a, Danielle R. Monteverde^a, John S. Magyar^a, Samuel M. Webb^d, Joan Selverstone Valentine^{a,e,1}, Brian M. Hoffman^c, and Woodward W. Fischer^a

^aDivision of Geological and Planetary Sciences, California Institute of Technology, Pasadena, CA 91125; ^bLos Alamos National Laboratory, Los Alamos, NM 87545; ^cDepartment of Chemistry, Northwestern University, Evanston, IL 60208; ^dStanford Synchrotron Radiation Lightsource, Stanford University, Menlo Park, CA 94025; and ^eDepartment of Chemistry and Biochemistry, University of California, Los Angeles, CA 90095

Contributed by Joan Selverstone Valentine, May 3, 2021 (sent for review December 7, 2020; reviewed by Valeria Cizewski Culotta and Kenneth H. Nealson)

Desert varnish is a dark rock coating that forms in arid environments worldwide. It is highly and selectively enriched in manganese, the mechanism for which has been a long-standing geological mystery. We collected varnish samples from diverse sites across the western United States, examined them in petrographic thin section using microscale chemical imaging techniques, and investigated the associated microbial communities using 16S amplicon and shotgun metagenomic DNA sequencing. Our analyses described a material governed by sunlight, water, and manganese redox cycling that hosts an unusually aerobic microbial ecosystem characterized by a remarkable abundance of photosynthetic Cyanobacteria in the genus *Chroococcidiopsis* as the major autotrophic constituent. We then showed that diverse Cyanobacteria, including the relevant *Chroococcidiopsis* taxon, accumulate extraordinary amounts of intracellular manganese—over two orders of magnitude higher manganese content than other cells. The speciation of this manganese determined by advanced paramagnetic resonance techniques suggested that the Cyanobacteria use it as a catalytic antioxidant—a valuable adaptation for coping with the substantial oxidative stress present in this environment. Taken together, these results indicated that the manganese enrichment in varnish is related to its specific uptake and use by likely founding members of varnish microbial communities.

rock varnish | desert varnish | Cyanobacteria | manganese | oxidative stress

Rock varnish (also called desert varnish) is a thin, dark coating found on exposed surfaces of rocks in arid environments that is composed primarily of clay minerals and manganese and iron oxides (1–3). It has long been recognized as a geochemical puzzle (4–6) and has received considerable scientific and popular interest due to its widespread occurrence (7), association with archaeological petroglyphs (8–10), use in age dating (11–17), potential as a paleoclimate proxy (16, 18–20), and comparisons to rock coatings on Mars (21–24). However, many interpretations and applications of varnish hinge on understanding the mechanism of its formation, which remains unknown.

The most perplexing aspect of varnish is its extremely high enrichment in manganese. Varnish characteristically contains 10–30 wt% MnO—two to three orders of magnitude higher manganese content than typical underlying rocks or the surrounding dust from which much of the mass comprising varnish originates (2, 3, 25). Other major elements including iron, silicon, aluminum, magnesium, sodium, and titanium, although abundant, are not enriched.

Diverse microorganisms are known to be associated with varnish, but whether or not they play a role in its origin has been fiercely debated (26). Numerous processes, both abiotic (e.g., dust deposition, water leaching, photochemical manganese oxidation) and biological (e.g., microbial mediation of binding and cementation, microbial manganese oxidation), have been proposed to contribute (summarized in *SI Appendix, Text*), but since varnish grows very slowly—at most tens of microns over a thousand years (27)—empirical demonstration has not been attainable. While many of these processes

may be relevant to varnish formation, none of them satisfactorily explains the highly and selectively enriched manganese content in varnish.

In this paper, we stepped back from the various paradigms that have been previously proposed and considered varnish formation from a holistic perspective. Synthesizing results from physical, chemical, and biological analyses, we reevaluated the relationship between varnish microflora and their environment and developed a hypothesis linking specific manganese accumulation to environmental adaptations of major members of the varnish microbial community.

Results

Varnish Is Governed by Sunlight, Water, and Manganese Redox Cycling.

We collected varnish on a range of rock types from seven field areas across the western United States (*SI Appendix, Fig. S1*). Varnish occurs on diverse lithologies in different settings, yet there are some common developmental patterns. A close relationship between varnish and sunlight has been established—varnish develops preferentially on lit rather than shaded surfaces (28–30). Although found in arid environments, therein varnish develops preferentially with the availability of water, such as in shallow depressions on rock surfaces where dew accumulates (31) and along runoff streaks down cliff faces (32). These observations provided circumstantial evidence that light and water play important roles in varnish formation.

Significance

Rock varnish is a prominent feature of desert landscapes and the canvas for many prehistoric petroglyphs. How it forms—and, in particular, the basis for its extremely high manganese content—has been an enduring mystery. The work presented here establishes a biological mechanism for this manganese enrichment, underpinned by an apparent antioxidant strategy that enables microbes to survive in the harsh environments where varnish forms. The understanding that varnish is the residue of life using manganese to thrive in the desert illustrates that, even in extremely stark environments, the imprint of life is omnipresent on the landscape.

Author contributions: U.F.L., C.M.Y., N.L.L., J.S.V., and W.W.F. designed research; U.F.L., C.M.Y., A.S., N.L.L., D.P.M., A.D.A., D.R.M., J.S.M., S.M.W., B.M.H., and W.W.F. performed research; U.F.L., C.M.Y., A.S., G.X., G.L.C., and B.M.H. analyzed data; and U.F.L., J.S.V., and W.W.F. wrote the paper.

Reviewers: V.C.C., Johns Hopkins University; and K.H.N., University of Southern California.

The authors declare no competing interest.

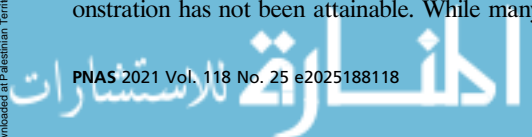
This open access article is distributed under [Creative Commons Attribution-NonCommercial-NoDerivatives License 4.0 \(CC BY-NC-ND\)](https://creativecommons.org/licenses/by-nc-nd/4.0/).

See [online](#) for related content such as Commentaries.

¹To whom correspondence may be addressed. Email: usha@caltech.edu or jsv@chem.ucla.edu.

This article contains supporting information online at <https://www.pnas.org/lookup/suppl/doi:10.1073/pnas.2025188118/-DCSupplemental>.

Published June 14, 2021.



To understand better the physical processes controlling varnish development, we examined depositional textures in petrographic thin sections using backscatter scanning electron microscopy (SEM). Varnish cross-sections revealed micrometer-scale, sub-horizontal laminations that reflect its accretionary mode of growth (Fig. 1B and SI Appendix, Fig. S2) (3). In all varnish samples examined, we observed laminae with crinkly to columnar or domal textures that mark an emergent topography similar to that of stromatolites—macroscopic sedimentary structures commonly understood as mineralized residue of ancient microbial mats (33). In certain stromatolites, these textures have been interpreted in terms of light-dependent growth, models of which come from studies of coral growth (34). On a topographically irregular surface, relative highs receive more light while relative lows get shaded; thus, the highs grow higher forming columnar features. In varnish, these microtextures supported the relationship with sunlight that has been documented with macroscale field observations and strengthened the evidence for a role for light in varnish genesis.

Textural data also supported the previously documented relationship with water by suggesting that varnish formation involves manganese redox cycling through a soluble phase. Desert dust samples that we collected at varnish sites contained manganese as both trace Mn^{2+} in igneous minerals and manganese oxide particles (SI Appendix, Fig. S2E). We observed detrital particles embedded in varnish, but high-resolution chemical imaging by energy dispersive spectroscopy (EDS) and nanoscale secondary ion mass spectrometry

(NanoSIMS) showed that these particles are largely silicate minerals, while the manganese-rich oxide material that characterizes varnish is in the laminated cement itself (SI Appendix, Figs. S3 and S4). Since manganese is water soluble in its divalent form but not as higher-valent oxides, redox cycling is required to mobilize and reprecipitate the manganese oxide in dust to form the accreting oxide cements.

The manganese oxide mineral phase in varnish has been described as poorly crystalline birnessite (2)—a phase composed of manganese octahedra organized in layers (35); it is formally $Mn^{4+}O_2$, but can incorporate a substantial fraction of Mn^{3+} instead of Mn^{4+} when accompanied by charge balance with heteroatoms (Na^+ , K^+ , Ba^{2+} , etc.) between the layers (36). Using synchrotron X-ray absorption near-edge structure (XANES) spectroscopy and multiple-energy “redox” mapping at the manganese K-edge, we found that varnish birnessite is not homogenous in its redox properties. Although predominantly Mn^{4+} , it contains common discrete microscale domains with variable and considerable mixtures of Mn^{3+} (Fig. 1C–E and SI Appendix, Fig. S2). This heterogeneity is consistent with the view that manganese redox cycling occurs within varnish, and the distribution of these domains indicates that such cycling is not restricted to surficial processes contributing to the ongoing accretion of varnish, but rather also characterizes the ecosystem that exists within well-developed varnish.

Numerous manganese redox cycling processes occur in Earth surface environments. Manganese oxidation with atmospheric O_2

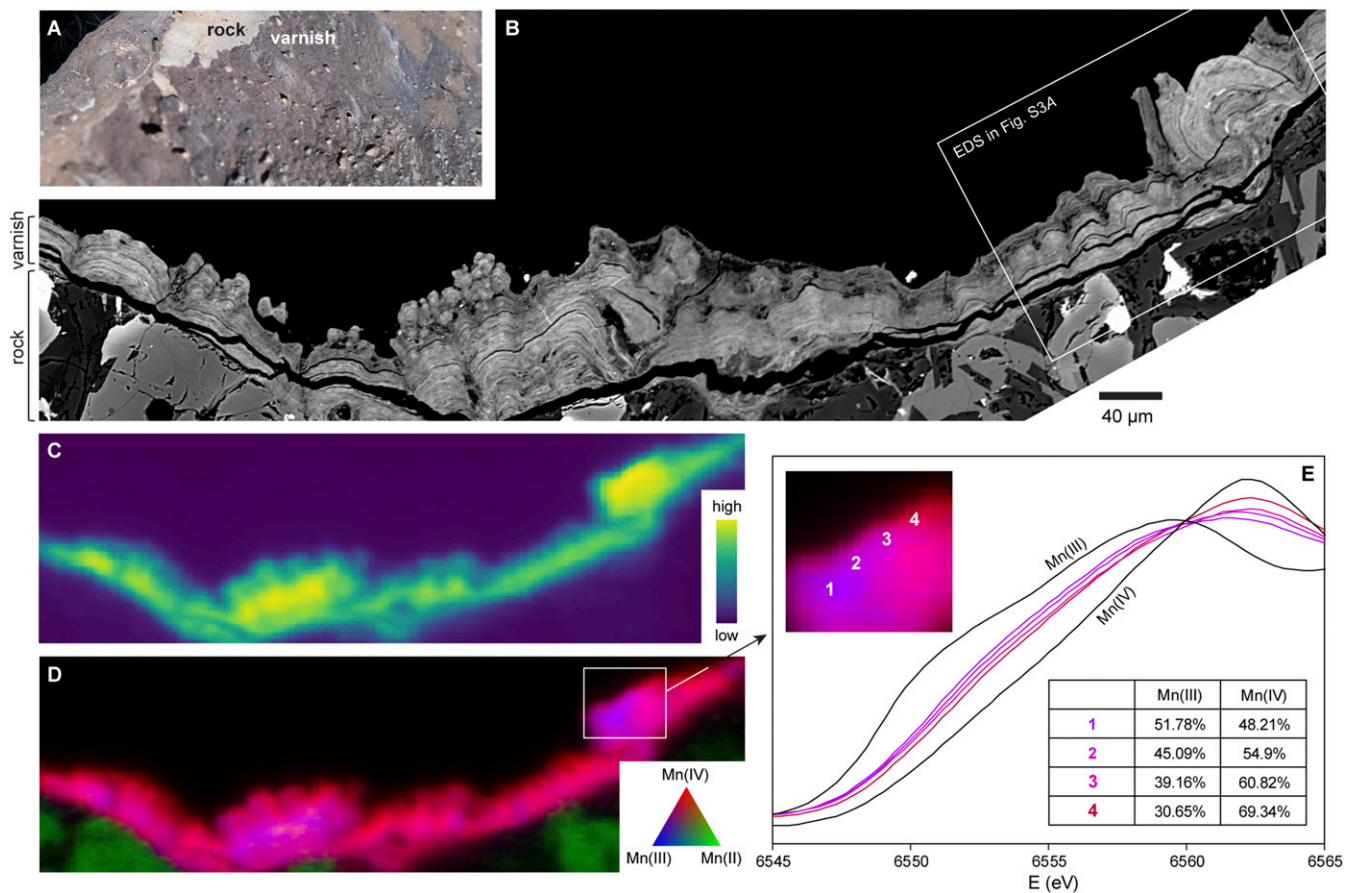


Fig. 1. Stromatolitic microtextures and manganese redox states in varnish developed on a basalt flow at Babbitt Ranch, AZ. (A) Photograph of varnished surface with a freshly broken face revealing underlying rock. (B) SEM image of a cross-section through the varnish–rock interface showing accretionary laminations that establish stromatolitic columns and domes. (C) Synchrotron X-ray microprobe map showing manganese distribution. Varnish is massively enriched in manganese relative to underlying rock. (D) Manganese redox map. Manganese in basalt is entirely Mn^{2+} , while varnish is predominantly Mn^{4+} with spatially varying domains richer in Mn^{3+} . (E) Point spectra taken across a manganese redox gradient. *Inset* table shows least-squares fits quantifying the components of each spectrum.

is thermodynamically favorable and can be catalyzed by metal oxide surfaces or bacterial and fungal enzymes (37–40). Manganese reduction can also be catalyzed by microbial processes, notably anaerobic respiration (41), and with an appropriate electron donor present (e.g., organic carbon) photochemical reduction of manganese oxides occurs readily even in aerobic settings (42–44). While any of these processes might contribute to varnish development and the manganese redox heterogeneity we observed, the relationship between varnish and sunlight raised the hypothesis that photochemistry—and perhaps photobiology—might play particularly important roles.

To visualize organic matter in varnish, we used NanoSIMS imaging of sulfur. ^{32}S appeared throughout varnish, notably concentrated in micrometer-scale particles that sit along varnish laminations and are distinct from detrital grains observed in the ^{28}Si and ^{57}Fe mass channels (SI Appendix, Fig. S4A). To confirm that this sulfur reflects organics rather than just sulfur-bearing mineral phases, we used XANES spectroscopy to assess electronic structure at the sulfur K-edge. The sulfur in varnish displayed complex speciation; sulfur is present in organic forms observed in biological material (variable mixtures of thiols with disulfides, sulfoxides, and sulfonates) as well as sulfate salts (SI Appendix, Fig. S4B). The fact that varnish is rich in organics and exposed to light—conditions that promote manganese photoreduction—and yet the manganese is maintained largely as Mn^{4+} oxides supports the view that dynamic redox cycling occurs within varnish.

The Varnish Microbial Community Is Characterized by Cyanobacteria.

To investigate the microbial diversity in varnish, we extracted DNA from varnish samples along with samples of surrounding surface soils for comparison. 16S rRNA gene amplicon sequencing revealed a varnish-specific microbial community that is distinct from surrounding soils, but common among varnishes from different rock types and locations (SI Appendix, Figs. S5–S7). The taxa we recovered are consistent with previous studies of varnish microbiology (45–48), with the bacterial families Xenococcaceae, Rubrobacteraceae, Acetobacteraceae, Sporichthyaceae, and Gemmatimonadaceae distinguishing the varnish community.

The most striking observation from our community analyses was the high abundance of Cyanobacteria associated with varnish, specifically members of *Chroococcidiopsis*—a genus of the family Xenococcaceae noted for its ability to live in extreme environments, with high tolerance for radiation and desiccation (49–52) (Fig. 2). 16S sequences assigned to the Xenococcaceae (either *Chroococcidiopsis* or unassigned below the family level) were recovered from 48 out of 49 varnish samples and accounted for 25.9% of all sequence reads and 98.7% of cyanobacterial reads recovered from varnish. In contrast, the Xenococcaceae represented only 0.06% of all reads and 1.4% of cyanobacterial reads from soil. The single most abundant unique *Chroococcidiopsis* sequence variant accounted for 8% of all reads from varnish and was completely absent from soil samples. Top BLAST hits for this sequence in the National Center for Biotechnology Information (NCBI) nr database included a remarkable representation of hits from previous varnish studies, and 99.6% identity with isolate Ryu 1–3 from the University of the Ryukyus in Okinawa, Japan (53), which we obtained for further study. Additionally, epifluorescence microscopy on varnish flakes revealed sarcinoid clusters of cells that are morphologically characteristic of baecocystous *Chroococcidiopsis* cells (Fig. 2D).

Shotgun metagenomic sequencing of select samples further emphasized the importance of these Cyanobacteria in the varnish community. In total, 21.9% of raw metagenome reads were assigned to Cyanobacteria, corroborating their high abundances in the 16S amplicon data (SI Appendix, Fig. S6C). We recovered six high-quality cyanobacterial metagenome-assembled genomes (MAGs), all belonging to members of the Chroococcidiopsidaceae (SI Appendix, Fig. S8). These Cyanobacteria appeared to be the main primary

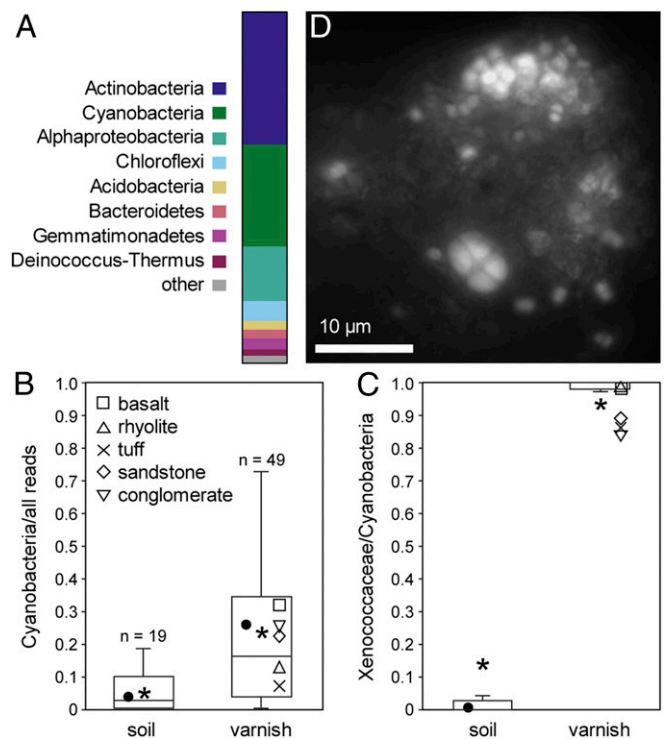


Fig. 2. Cyanobacteria of the family Xenococcaceae are a major and specific constituent of the varnish microbial community. (A) Average taxonomic composition of varnish communities by 16S rRNA gene amplicon sequencing. (B and C) Box-and-whisker plots showing the abundance of Cyanobacteria (B) and family Xenococcaceae within the Cyanobacteria (C) in 16S reads from varnish vs. neighboring soil samples. The filled circles indicate fraction of all reads, asterisks indicate average relative abundance of all samples, and other shapes indicate average relative abundance of each varnished rock type. (D) Fluorescence microscopy highlighting cells with the characteristic sarcinoid morphology of *Chroococcidiopsis* in varnish.

producers of the varnish community—of nine MAGs containing genes for the Calvin–Benson–Bassham cycle, six were Cyanobacteria, with three others representing considerably less abundant taxa (of Armatimonadota, Rhodobacteraceae, and Beijerinckiaceae). No MAGs appeared to encode alternative carbon fixation pathways. Furthermore, we only recovered one additional MAG with phototrophic reaction center genes (an aerobic photoheterotroph of the Acetobacteraceae), indicating that the Cyanobacteria are the only taxa in varnish capable of using light as an energy source for autotrophic growth. Sulfur K-edge spectra of *Chroococcidiopsis* cells were similar to the organic content we observed within varnish (SI Appendix, Fig. S4), supporting the interpretation that these taxa are the main primary producers of the ecosystem.

By both abundance and function, we concluded that *Chroococcidiopsis* are extremely important taxa in varnish and are likely founding autotrophic members of the community. When considered in this context, the physical evidence that sunlight and water play important roles in varnish development can be interpreted to suggest that these Cyanobacteria, which grow with light and water, might be involved in the formation of varnish itself.

Metagenomic data also revealed that the varnish microbial communities mark a highly aerobic ecosystem, far more so than typical sediments or soils. No obligate anaerobic metabolisms were represented by the gene content of our MAGs—consistent with the known physiologies of the major taxa identified in our 16S analysis. Indeed, nearly all MAGs contained high-potential bioenergetic systems utilized in aerobic respiration as well as reactive oxygen species detoxification systems. Of the 38 MAGs

we recovered from varnish samples, we observed heme-copper O_2 reductase and/or *bd* O_2 reductase complexes in 37 of them, a superoxide dismutase in 34 of them, and a catalase in 24 of them. These aerobic adaptations are unsurprising considering the proximity of this community to atmospheric O_2 and exposure to solar irradiation; they are biochemical attestations to the high degrees of oxidative stress encountered in this harsh environment.

Cyanobacteria Accumulate Manganese Likely as a Nonenzymatic Antioxidant System. The significance of cyanobacterial taxa as abundant keystone members of the varnish ecosystem suggested to us a previously unexplored connection between the microbial community and the manganese content of varnish. The model freshwater cyanobacterium *Synechocystis* sp. PCC 6803 has been shown to accumulate a massive pool of intracellular Mn^{2+} , up to 10^8 atoms per cell, which when averaged over cell volume is the equivalent concentration of 100 mM manganese—four orders of magnitude higher than their growth medium (54). We hypothesized that if this hyperaccumulation of manganese occurs broadly in the Cyanobacteria—particularly those taxa that are dominant members of the varnish community—then this physiological peculiarity might underpin varnish development.

We examined two strains of *Chroococcidiopsis* (PCC 7433 and Ryu 1–3, the closest cultured relative to the varnish sequences), *Synechocystis* sp. PCC 6803, and *Gloeobacter violaceus* PCC 7421, a very deep branching member of the photosynthetic Cyanobacteria (SI Appendix, Fig. S9), along with noncyanobacterial model organisms *Escherichia coli* K12 and *Shewanella oneidensis* MR-1 for comparison. Using inductively coupled plasma mass spectrometry (ICP-MS) to measure total cellular manganese, we observed dramatic manganese accumulation in all cyanobacterial strains; the highest values were seen in Ryu 1–3, with over two orders of magnitude greater manganese content than that seen in *E. coli* or *S. oneidensis* (Fig. 3A).

To probe the speciation of this copious intracellular manganese, we combined electron paramagnetic resonance (EPR), electron nuclear double resonance (ENDOR), and electron spin echo envelope modulation (ESEEM) spectroscopies. The EPR spectra of all Cyanobacteria examined showed that the majority of the Mn^{2+} pool exists in soluble high-symmetry complexes with low-molecular-weight ligands (denoted H- Mn^{2+}) and not in low-symmetry complexes with strongly chelating ligands or bound to proteins (denoted L- Mn^{2+}) (Fig. 3B and SI Appendix, Fig. S10A and B). ^{31}P , 1H ENDOR, and ^{14}N ESEEM measurements along with ^{13}C ENDOR on labeled cells further revealed that this manganese binds undetectably low amounts of phosphate and nitrogenous ligands, and is instead predominantly bound to carboxylato ligands (Fig. 3C and SI Appendix, Fig. S10C and D and Text). Notably, previously studied organisms with abundant cellular H- Mn^{2+} exhibited significant contributions from phosphate and nitrogenous ligands (55, 56); this difference makes the Mn^{2+} pool in Cyanobacteria distinct.

This speciation data implied the functional role for Mn^{2+} in cyanobacterial physiology as a small-molecule antioxidant system. Certain H- Mn^{2+} complexes are known to act as effective catalytic antioxidants of superoxide and peroxide (57, 58), and accumulation of H- Mn^{2+} has been shown to predict oxidative stress resistance (55, 59). This physiology is well documented in radiation-resistant taxa such as *Deinococcus radiodurans* (60, 61), but was not previously known in Cyanobacteria. The H- Mn^{2+} accumulation shown here helps explain how the Cyanobacteria in varnish cope with the extremely aerobic, arid, and irradiated environments where varnish is found. Taken together with the high abundance of cyanobacterial taxa associated with varnish, the establishment of this cyanobacterial manganese-based antioxidant system provides an adaptive biological mechanism behind the enrichment of manganese in rock varnish.

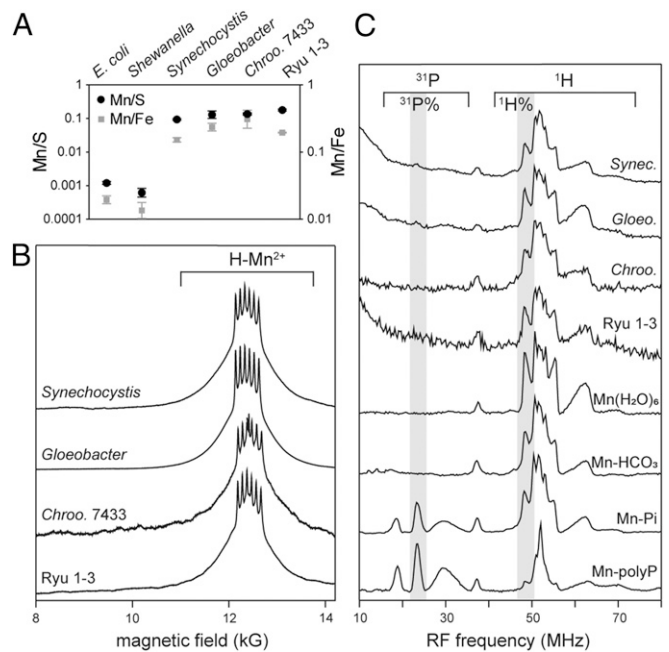


Fig. 3. Cyanobacteria accumulate substantial intracellular Mn^{2+} , predominantly coordinated by small-molecule carboxylato ligands. (A) Cellular manganese abundance measured by ICP-MS, reported as a ratio to sulfur as a proxy for normalizing to biomass, and to iron—a metric commonly associated with oxidative stress tolerance. Results are means of measurements from three independent cultures; error bars reflect SE. (B) Absorption-display 35-GHz 2 K CW EPR spectra showing that >95% of cyanobacterial Mn^{2+} exists as H- Mn^{2+} complexes. (C) The 35-GHz 2 K $^{31}P/^1H$ Davies pulsed ENDOR spectra of Cyanobacteria and Mn^{2+} standards. Braces represent spans of ^{31}P and 1H ENDOR responses; $^{31}P\%$ and $^1H\%$ represent absolute ENDOR responses (gray highlight). The negligible $^{31}P\%$ ENDOR signals and diminished $^1H\%$ ENDOR responses of Cyanobacteria vs. hexaquo Mn^{2+} indicate that >90% of the cyanobacterial Mn^{2+} is bound to ENDOR-silent carboxylato ligands (represented by $Mn-HCO_3$ standard), which was confirmed by ENDOR measurements of ^{13}C -labeled cells (SI Appendix, Fig. S10D).

Discussion

Varnish develops in environments that are extremely harsh, where protective strategies against irradiation and oxidative stress are essential for life to survive. The presence of the varnish microbial community has been noted in such terms; for example, varnish provides a habitat for microbial life shielded by oxide minerals that absorb UV radiation (62). However, up until now, how and why the varnish—with its high and specific enrichment in manganese—got there in the first place was a mystery. Based on the data presented here, we propose that varnish itself is a hallmark of life prevailing in these extreme environments.

We showed that Cyanobacteria of the genus *Chroococcidiopsis* are intimately and abundantly associated with varnish. Moreover, being the main primary producers of the ecosystem, these organisms must establish prior to heterotrophic taxa that depend upon them for organic substrates, implicating them as likely founding members of the microbial community. Evidence tying sunlight and water to varnish development provided further, albeit circumstantial, evidence that photosynthetic Cyanobacteria play a fundamental role. We then demonstrated that diverse Cyanobacteria, including *Chroococcidiopsis*, accumulate substantial quantities of H- Mn^{2+} . This phenomenon is well established as an antioxidant strategy that enables tremendous oxidative stress resistance (58, 59, 63); indeed, there is no other known physiological purpose for such elevated manganese concentrations. The cyanobacterial H- Mn^{2+} pool that we observed is comparable in magnitude to the most radiation-resistant organisms known (60).

Many previous studies have focused on a mechanism of manganese oxidation as the key to varnish formation. However, in such aerobic environments, manganese oxidation may proceed through numerous pathways with both biological (*SI Appendix, Text and Fig. S8*) and abiotic (including photochemical and autocatalytic) mechanisms. Rather than oxidation, we argue that it is the selective enrichment of manganese that represents a process of singular importance to the development of varnish. The manganese hyperaccumulation that we observed in *Chroococcidiopsis* provides a simple and effective, ecologically relevant, physiological explanation for this manganese enrichment.

Thus, we propose a hypothesis for varnish formation (Fig. 4). These Cyanobacteria grow on sunlit rock surfaces with intermittent access to water, sequestering high concentrations of manganese in their cells and exploiting the unique redox chemistry of manganese complexes as a catalytic antioxidant system that enables their survival in such a harsh environment. When they die, the residue from their biomass provides an enriched manganese source that is ultimately oxidized to form the oxide mineral cements that comprise varnish. Since varnish forms over timescales of millennia, a well-developed varnish sample represents the time integrated manganese accumulation of many, many generations of cells, which are sparsely distributed at any given time. This was demonstrated in our analyses of varnish samples in petrographic thin section—the Mn^{2+} content of any living cells is negligible next to thousands of years of accumulated Mn^{3+}/Mn^{4+} mineral. In addition to solving the mystery of manganese enrichment, cyanobacterial exudates and necromass also supply fresh organic carbon to the varnish ecosystem. This provides a growth substrate for the heterotrophic microbes that inhabit varnish, as well as an effective electron donor for photochemical manganese reduction. Taken together, our results place the activity of extremophilic Cyanobacteria as a key driver of both the physical and biological development of varnish ecosystems.

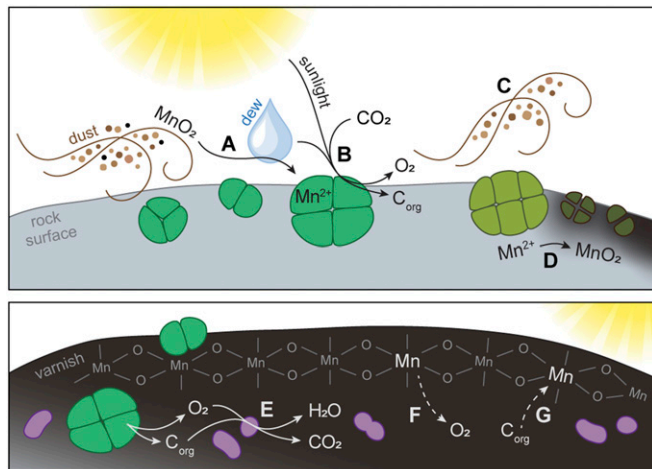


Fig. 4. Natural history of varnish. (A) Manganese is delivered largely as oxide particles in windborne dust, reduced by either photochemical or biological processes, and taken up by *Chroococcidiopsis* cells for use as a catalytic antioxidant. (B) *Chroococcidiopsis* grows with light and water, fixing carbon and trapping accumulated manganese. (C) Dust material not adhered to the rock surface is removed by wind or precipitation. (D) When *Chroococcidiopsis* cells die, the manganese-rich residue left behind by their biomass is oxidized to generate the manganese oxides that comprise varnish. This oxidation can be biologically catalyzed and/or abiotic. (E) Products from cyanobacterial photosynthesis serve as substrates for heterotrophic community members. (F and G) Manganese redox cycling continues in developed varnish, with abundant O_2 as an electron acceptor (F) and organic matter as an electron donor (G).

Methods

Study Locations and Sampling. Samples were taken from seven field locations across the southwestern United States, ranging from arid to semiarid climates, corresponding to rock varnish Type I and Type II designated by Macholdt et al. (64) (*SI Appendix, Fig. S1*). Underlying lithologies including mafic, felsic, and sedimentary rocks. Varnished rocks were collected with ethanol-sterilized gloves into Whirl-Pak sample bags, and surface soil samples were collected using sterile spatulas into falcon tubes. Ultrathin sections cut orthogonal to the varnished surface were prepared by David Mann at High Mesa Petrographics (Los Alamos, NM). The thin sections revealed varnishes ranging in thickness from ~5 to ~100 μm , likely representing hundreds to thousands of years of development (27). For DNA sampling, varnished rocks were returned to the laboratory, gently rinsed with sterile nanopure water using a 50-mL syringe and 16-gauge needle, and allowed to dry. For DNA extraction, varnish was removed from rock surfaces by scraping with flame-sterilized steel brushes, spatulas, and dental picks, and collected in a weigh boat. Each varnish sample was obtained from a separate rock. Dust analysis was conducted on a fine grained (clay-silt sized) fraction of surface soil from the Barstow field location.

SEM/EDS/NanoSIMS. SEM and EDS analyses were conducted in the Caltech Geological and Planetary Sciences Division Analytical Facility on a ZEISS 1550VP Field Emission SEM, with a Robinson-type backscatter electron detector and an Oxford X-Max SDD X-ray EDS system. Varnish was imaged at 10–20 kV with working distances of 7–10 mm and magnifications of 500–4,500 \times . NanoSIMS analyses were conducted in the Caltech Microanalysis Center, on a Cameca NanoSIMS 50L using a Cs^+ primary ion beam with 50-nm resolution, primary ion current of 1 pA, and dwell time of 3.5 ms/pixel. The masses of ^{12}C , ^{14}N , ^{32}S , ^{31}P , ^{18}O , ^{28}Si , ^{55}Mn , ^{16}O , and ^{57}Fe were collected. Petrographic thin sections were coated with 20-nm graphite using a Turbo carbon evaporator for SEM/EDS, and with 40-nm gold using a Cressington HR metal sputtering coater for NanoSIMS. EDS and NanoSIMS images were examined using ImageJ.

Synchrotron X-Ray Spectroscopy. Synchrotron analyses were conducted at the Stanford Synchrotron Radiation Lightsource, on X-ray microprobes at beamlines 2–3 for the manganese K-edge and 14–3 for the sulfur K-edge. The 2–3 beam was energy calibrated using the pre-edge feature of $KMnO_4$ at 6,543.34 eV, and 14–3 was calibrated using the pre-edge feature of $Na_2S_2O_3$ at 2472.02 eV. Multiple energy maps for producing images of manganese redox state were collected at 6,553, 6,557, 6,559, 6,562, and 6,570 eV, with 3- μm resolution. For both spectra and maps, least-squares fitting was done using a spersartine standard spectrum (65) representative of igneous Mn^{2+} , manganic oxide (65), and feitknechtite (66) standard spectra as two different Mn^{3+} -bearing phases, and an internal endmember spectrum for $Mn^{4+}O_2$. Spectra and maps were reduced and fit using the SIXPACK (67) and SMAK (68) software packages, respectively (<https://www.sams-xrays.com/>). Colormaps were converted to viridis using fixthejet (<https://fixthejet.eclife.org/>).

DNA Extraction and Sequencing. Genomic DNA was extracted from 10 to 50 mg varnish scrapings or soil using the FastDNA SPIN kit for soil (MP Bio-medicals). DNA yields were quantified using a Qubit 2.0 fluorometer with the HS dsDNA assay kit (Thermo Fisher Scientific).

To generate 16S rRNA gene libraries, the V3–V4 hypervariable region of the 16S gene was amplified using degenerate primers (341–806 pair) from ~12.5 ng of genomic DNA with KAPA HiFi HotStart ReadyMix (denaturation at 95 $^{\circ}C$ for 3 min, 20 cycles of 95 $^{\circ}C$ for 30 s, 55 $^{\circ}C$ for 30 s, and 72 $^{\circ}C$ for 30 s, and a final extension of 72 $^{\circ}C$ for 5 min before holding at 4 $^{\circ}C$). A second round of PCR added Nextera XT v2 indexes (Illumina) (denaturation at 95 $^{\circ}C$ for 3 min, 8 cycles of 95 $^{\circ}C$ for 30 s, 55 $^{\circ}C$ for 30 s, and 72 $^{\circ}C$ for 30 s and a final extension of 72 $^{\circ}C$ for 5 min before holding at 4 $^{\circ}C$). The amplicons were cleaned up using AMPure XP beads (Beckman Coulter). A no-template control was processed and did not show a band in the amplicon region. The amplicons were pooled and sequenced on the Illumina MiSeq platform generating paired end 301-bp reads using the MiSeq reagent kit v3 (600 cycles) (Illumina).

Two representative varnish DNA samples (sample 24, sandstone from Babbitt Ranch, AZ, and sample 41, basalt from Mesa Prieta, NM) were selected for metagenomic sequencing. These samples were selected based on 16S amplicon data as likely candidates to recover high-quality genomes for the major taxa in the varnish community. No aspects of the communities in these two samples were outliers, and together they represent samples from two different locations and very different rock types.

Illumina shotgun libraries were prepared using the Next Ultra DNA II library preparation kit (New England Biolabs). DNA was fragmented using a Covaris E220; the ends were made blunt and adapters and indexes added

onto the fragments to generate Illumina libraries, which were eluted in DNA elution buffer (Zymo). Libraries were quantified using the KAPA Illumina/Universal library quantification kit, normalized based on qPCR results, and sequenced on the Illumina NextSeq platform generating paired end 151-bp reads using the NextSeq 500/550 high output kit v2.5 (300 cycles) (Illumina).

16S Data Processing. 16S amplicon sequence reads from 61 varnish samples and 19 soil samples were processed using QIIME2 (69) to generate feature tables containing the frequencies of each unique sequence variant per sample. Quality filtering, denoising, merging of paired end reads, and chimera removal were done using DADA2 (70). The QIIME2 q2-feature-classifier plugin was used to align the sequences against the Greengenes 13.8 database (71) and assign taxonomy. One sample that returned <2,000 total reads was omitted from downstream analyses. NMDS and ANOSIM analyses were done by calculating a Bray dissimilarity matrix using the vegan ecology package in R (72). LEfSe analysis was done using the Microbiome Analyst tool (73) with default settings. For the phylogenetic tree presented in this paper, sequences were aligned with the SINA aligner (74) and converted from fasta format to phylip format with SEAVIEW (75). The phylogenetic tree was constructed using PhyML (76) implemented on the website www.atgc-montpellier.fr/phyml/ with default settings, and the resulting tree was visualized using FigTree.

Metagenomic Data Processing. Taxonomic assignments of raw metagenome reads were done using the MG-RAST analysis platform (77). Metagenome sequence read quality control, de novo assembly, and binning of MAGs was performed largely on the KBase platform (78). Combinations of read preprocessing, assembly, and binning methods were tested and evaluated based on the quality and quantity of final MAGs. Read preprocessing included no processing (raw reads), Bloom Filter Read Error Correction (79) v. r181 (drop_unique_kmer_reads = 1, kmer_size = 33), Trimmomatic (80) v. 0.38 (LEADING:3 TRAILING:3 SLIDINGWINDOW:4:15 MINLEN:125), and BMap (81) v37.93 (bbduk.sh -Xmx1g, k = 15, mink = 10, ktrim = r, tbo). Processed reads were assembled with MEGAHIT (82) v2.4.2 (metalarge), MetaSPAdes (83) v1.2.4 (K-mer sizes 33, 55, 77, 99, and 127), or IDBA-UD (84) v1.0.4. Assemblies were performed with minimum contig size of 2,000 bp. MAGs were constructed with two automated binning tools, MaxBin2 (85) v2.2.4 and MetaBAT2 (86) v1.7 with default settings except for minimum contig lengths of 2,500 bp. All MAGs from combinations of the above setting were evaluated for quality using the CheckM software v1.0.18 on KBase with default settings. Sufficiently high-quality bins were defined using the Parks et al. (87) cutoff of completeness—5*contamination > 50. Bin taxonomy was assigned using GTDB-Tk v0.3.2 using gtdbtk release 89 (88). The number of bins passing this cutoff and their phylogenetic affiliations were used to compare between the different parameters described above. The greatest number of quality bins was achieved with Trimmomatic, MetaSPAdes, and MetaBAT2 for sample 41, and Trimmomatic + Bmap mink, MetaSPAdes, and MetaBAT2 for sample 24. Other combinations of parameters produced a subset of less complete versions of the final bins, not completely different MAGs. Genome annotation was conducted using the RASTtk algorithm (89) v.0.1.1 in KBase, as well as a local implementation of the KofamScan (90) software for the KEGG database. The canonical metabolic pathways encoded by these genomes were parsed using KEGG-decoder (91), and additional analyses of genes of interest, including MCOs and pili, were done using local BLAST searches for known systems (*SI Appendix, Supplementary Material*). Cytochromes *c* were identified by counting heme-binding domains (CxxCH motifs), and beta barrels were predicted using the PRED-TMBB tool (92).

Fluorescence Microscopy. Fluorescence microscopy was performed at the Center of Integrated Nanotechnologies at Los Alamos National Laboratory. Cavity well microscope slides (Globe Scientific) were used to mount varnish flakes and fitted with #1.5 coverslips. Imaging was conducted on a Zeiss Axio Observer D1 inverted microscope equipped with a 100 \times , 1.3 N.A. oil-immersion objective and a BP 640/30 excitation and BP 690/50 emission filter set to observe chlorophyll autofluorescence.

Culture Conditions. *Synechocystis* sp. PCC 6803 (obtained from Richard Debus, University of California, Riverside, CA), *Gloeobacter violaceus* PCC 7421 (obtained from ATCC), *Chroococcidiopsis cubana* PCC 7433 (obtained from ATCC), and Ryu 1–3 (obtained from Shoichiro Suda, University of the Ryukyus), were grown in liquid BG11 medium (93), which contains 9 μ M MnCl₂. The 6803 and Ryu 1–3 were kept in a 30 $^{\circ}$ C shaking incubator under white fluorescent lights, and 7421 and 7433 were kept at room temperature with natural light on a windowsill. *E. coli* and *S. oneidensis* were grown in liquid LB medium, in a 30 $^{\circ}$ C shaking incubator. Cells were harvested after 24-h growth for *E. coli* and *S. oneidensis*, ~1 wk for 6803, and ~1 mo for 7421 and

7433. Ryu 1–3 was sufficiently slow growing that, once a month, all biomass in the culture was transferred to fresh medium.

ICP-MS. Harvested cells were washed in sterile nanopure water to remove residual media and any extracellular material, and then frozen at -80° C. Frozen cells were lyophilized in a SpeedVac vacuum concentrator, and the dried cell pellet was transferred to a 50-mL DigiTUBE (SCP Science). The dry cell pellet was digested for 2 h at 95 $^{\circ}$ C in 3 mL of concentrated (70%) nitric acid purified by distillation at Caltech. The digested cell pellet was then diluted to 50 mL with nanopure water. ICP-MS analysis was conducted in the Caltech Environmental Analysis Center on an Agilent 8800 ICP-MS Triple Quad using a collision/reaction cell with O₂ as the reaction gas. Sulfur was analyzed as ³²S¹⁶O (mass 48). Measurements were calibrated using a multi-element standard (Inorganic Ventures; IV-ICPMS-71A; Lot M2-MEB658498). Due to the extremely clumpy phenotype of the *Chroococcidiopsis* cells hindering accurate cell counts, manganese content was reported as a ratio to sulfur content as a proxy for normalizing to biomass. Cell-specific manganese abundance was determined for *Synechocystis* by cell counts in a Petroff Hausser counting chamber (Hausser Scientific).

EPR/ENDOR/ESEEM Spectroscopy. Concentrated cell suspensions in 40% glycerol were loaded into custom-made quartz EPR tubes, and then flash-frozen in liquid N₂. Paramagnetic resonance spectroscopy was conducted in the Hoffman Laboratory at Northwestern University. The 35-GHz continuous-wave (CW) EPR spectra were recorded using a laboratory-built EPR spectrometer (94). Absorption-display EPR spectra of frozen cells and manganese standards were collected in the “rapid passage” mode at 2 K as previously described (56, 59) (microwave [MW] frequency, 34.9 GHz; MW power, 1 mW; temperature, 2 K; modulation amplitude, 1 G; time constant, 64 ms; scan rate, 1 kG/min).

Pulsed ENDOR/ESEEM spectra were recorded using a laboratory-built 35-GHz pulsed EPR spectrometer (95). All spectra were recorded at 2 K using an immersion helium cryostat. ³¹P, ¹H Davies ENDOR spectra were recorded using the pulse sequence $\pi - T_{rf} - \pi/2 - \tau - \pi - \tau - \text{echo}$, where T_{rf} is the time interval for the radiofrequency (RF) pulse, which is randomly hopped (96) (MW frequency, 34.8 GHz; temperature, 2 K; magnetic field, ~12.5 kG; $t_{\mu/2} = 60$ ns; $\tau = 400$ ns; $T_{rf} = 160$ μ s; repetition time, 10 ms). The ENDOR response is enhanced by broadening the frequency-bandwidth of the RF pulse using a 100-kHz white noise source (97). ¹³C Mims ENDOR spectra were recorded using the pulse sequence $\pi/2 - \tau - \pi/2 - T_{rf} - \pi/2 - \tau - \text{echo}$ (MW frequency, 34.8 GHz; temperature, 2 K; magnetic field, ~12.5 kG; $t_{\mu/2} = 50$ ns; $\tau = 400$ ns; $T_{rf} = 20$ μ s; repetition time, 10 ms). Three-pulse ESEEM spectra were recorded using the pulse sequence, $\pi/2 - \tau - \pi/2 - T - \pi/2 - \tau - \text{echo}$, where T is the time varied between second and third MW pulses, with four-step phase cycling to suppress unwanted Hahn and refocused echoes (96) (MW frequency, 34.8 GHz; temperature, 2 K; magnetic field, ~12.5 kG; $t_{\mu/2} = 30$ ns; $\tau = 400$ ns; $T = 1$ μ s with 20-ns step size, repetition time of 10 ms).

Data Availability. Sequence data have been deposited as FASTQ files on the Sequence Read Archive (SRA) (BioProject ID [PRJNA630476](https://www.ncbi.nlm.nih.gov/bioproject/PRJNA630476)) (98). Binned genomes from samples 24 and 41 are available at CaltechDATA, <https://dx.doi.org/10.22002/D1.1960> (99).

ACKNOWLEDGMENTS. This research was supported by NSF Grant IOS-1833247 (U.F.L. and W.W.F.), NSF Graduate Research Fellowship Program (U.F.L.), NIH Grant GM111097 (B.M.H.), National Aeronautics and Space Administration Exobiology Grant 18-EXO18-0040 (W.W.F. and N.L.L.), and Los Alamos National Laboratory Laboratory-Directed Research and Development Project 20170414ER (C.M.Y. and N.L.L.). Use of the Stanford Synchrotron Radiation Lightsource (SSRL), SLAC National Accelerator Laboratory, was supported by the Department of Energy (DOE) Office of Basic Energy Sciences under Contract DE-AC02-76SF00515 and the SSRL Structural Molecular Biology Program supported by the DOE Office of Biological and Environmental Research and the NIH/National Institute of General Medical Sciences (Grant P41GM103393). This project benefited from the use of instrumentation made available by the Caltech Environmental Analysis Center, Caltech Microanalysis Center, and Caltech Geological and Planetary Sciences Division Analytical Facility. Fieldwork for this project was conducted on ancestral lands of the Hopi, Pueblo, Ute, Apsáalooke, and Serrano peoples. We thank George Rossman, Hope Johnson, Jared Leadbetter, and Yonaton Goldsmith for helpful discussions and insight; Chi Ma, Yunbin Guan, and Nathan Dalleska for help with SEM, NanoSIMS, and ICP-MS analyses; Nick Edwards and Sharon Bone for support at SSRL; Babbitt Ranches for allowing us to sample; Shoichiro Suda for supplying the Ryu 1-3 strain; and Jason Tor and the environmental microbiology class at Hampshire College for sparking U.F.L.’s interest in rock varnish research.

1. R. M. Potter, G. R. Rossman, Desert varnish: The importance of clay minerals. *Science* **196**, 1446–1448 (1977).
2. R. M. Potter, G. R. Rossman, The manganese- and iron-oxide mineralogy of desert varnish. *Chem. Geol.* **25**, 79–94 (1979).
3. R. S. Perry, J. B. Adams, Desert varnish: Evidence for cyclic deposition of manganese. *Nature* **276**, 489–491 (1978).
4. A. von Humboldt, *Personal Narrative of Travels to the Quinocentral Regions of America during the Years 1799–1804 by Alexander von Humboldt and Aime Bonpland* (Bell, London, 1812).
5. C. R. Darwin, *Journal of Researches into the Natural History and Geology of the Countries Visited during the Voyage of H.M.S. Beagle Round the World, under the Command of Capt. Fitz Roy, R.N* (John Murray, London, ed. 2, 1845).
6. A. Lucas, *The Blackened Rocks of the Nile Cataracts and of the Egyptian Deserts* (National Printing Department, 1905).
7. C. G. Engel, R. P. Sharp, Chemical data on desert varnish. *Geol. Soc. Am. Bull.* **69**, 487–518 (1958).
8. M. Dietzel, H. Kolmer, P. Pölt, S. Simic, Desert varnish and petroglyphs on sandstone—Geochemical composition and climate changes from Pleistocene to Holocene (Libya). *Geochemistry* **68**, 31–43 (2008).
9. D. S. Whitley, C. M. Santoro, D. Valenzuela, Climate change, rock coatings, and the archaeological record. *Elements* **13**, 183–186 (2017).
10. D. S. Whitley, *Cave Paintings and the Human Spirit: The Origin of Creativity and Belief* (Prometheus Books, 2009).
11. R. I. Dorn, Cation-ratio dating: A new rock varnish age-determination technique. *Quat. Res.* **20**, 49–73 (1983).
12. R. I. Dorn, P. B. Clarkson, M. F. Nobbs, L. L. Loendorf, D. S. Whitley, New approach to the radiocarbon dating of rock varnish, with examples from drylands. *Ann. Assoc. Am. Geogr.* **82**, 136–151 (1992).
13. P. R. Bierman, A. R. Gillespie, Evidence suggesting that methods of rock-varnish cation-ratio dating are neither comparable nor consistently reliable. *Quat. Res.* **41**, 82–90 (1994).
14. W. Beck, Ambiguities in direct dating of rock surfaces using radiocarbon measurements. *Science* **280**, 2132–2139 (1998).
15. A. Watchman, A review of the history of dating rock varnishes. *Earth Sci. Rev.* **49**, 261–277 (2000).
16. T. Liu, W. S. Broecker, Millennial-scale varnish microlamination dating of late Pleistocene geomorphic features in the drylands of western USA. *Geomorphology* **187**, 38–60 (2013).
17. D. S. Whitley, Rock art dating and the peopling of the Americas. *J. Archaeol.* **2013**, 1–15 (2013).
18. T. Liu, W. S. Broecker, J. W. Bell, C. W. Mandeville, Terminal Pleistocene wet event recorded in rock varnish from Las Vegas Valley, southern Nevada. *Palaeogeogr. Palaeoclimatol. Palaeoecol.* **161**, 423–433 (2000).
19. T. Liu, W. S. Broecker, Rock varnish evidence for latest Pleistocene millennial-scale wet events in the drylands of western United States. *Geology* **36**, 403–406 (2008).
20. Y. Goldsmith, Y. Enzel, M. Stein, Systematic Mn fluctuations in laminated rock varnish developed on coeval early Holocene flint artifacts along a climatic transect, Negev Desert, Israel. *Quat. Res.* **78**, 474–485 (2012).
21. R. S. Perry, V. M. Kolb, “From Darwin to Mars: Desert varnish as a model for preservation of complex (bio)chemical systems” in *Instruments, Methods, and Missions to Astrobiology VII*, R. B. Hoover, A. Y. Rozanov, Eds. (SPIE, 2004), vol. 5163, pp. 136–144.
22. D. Krinsley, R. I. Dorn, B. DiGregorio, Astrobiological implications of rock varnish in Tibet. *Astrobiology* **9**, 551–562 (2009).
23. N. L. Lanza et al., Examining natural rock varnish and weathering rinds with laser-induced breakdown spectroscopy for application to ChemCam on Mars. *Appl. Opt.* **51**, B74–B82 (2012).
24. N. L. Lanza et al., Understanding the signature of rock coatings in laser-induced breakdown spectroscopy data. *Icarus* **249**, 62–73 (2015).
25. Y. Goldsmith, M. Stein, Y. Enzel, From dust to varnish: Geochemical constraints on rock varnish formation in the Negev Desert, Israel. *Geochim. Cosmochim. Acta* **126**, 97–111 (2014).
26. R. I. Dorn, “Rock varnish” in *Geochemical Sediments & Landscapes*, D. J. Nash, S. J. McLaren, Eds. (Blackwell, 2007), pp. 246–297.
27. T. Liu, W. S. Broecker, How fast does rock varnish grow? *Geology* **28**, 183 (2000).
28. X. Xu et al., Characteristics of desert varnish from nanometer to micrometer scale: A photo-oxidation model on its formation. *Chem. Geol.* **522**, 55–70 (2019).
29. T. Waragai, Effects of rock surface temperature on exfoliation, rock varnish, and lichens on a boulder in the Hunza Valley, Karakoram Mountains, Pakistan. *Arct. Alp. Res.* **30**, 184 (1998).
30. A. Lu et al., Photoelectric conversion on Earth's surface via widespread Fe- and Mn-mineral coatings. *Proc. Natl. Acad. Sci. U.S.A.* **116**, 9741–9746 (2019).
31. C. E. Jones, Characteristics and origin of rock varnish from the hyperarid coastal deserts of northern Peru. *Quat. Res.* **35**, 116–129 (1991).
32. P. H. Larson, R. I. Dorn, Painting Yosemite Valley: A case study of rock coatings encountered at Half Dome. *Phys. Geogr.* **33**, 165–182 (2012).
33. T. Bosak, A. H. Knoll, A. P. Petroff, The meaning of stromatolites. *Annu. Rev. Earth Planet. Sci.* **41**, 21–44 (2013).
34. R. R. Graus, I. G. Macintyre, Light control of growth form in colonial reef corals: Computer simulation. *Science* **193**, 895–897 (1976).
35. J. E. Post, Manganese oxide minerals: Crystal structures and economic and environmental significance. *Proc. Natl. Acad. Sci. U.S.A.* **96**, 3447–3454 (1999).
36. F. T. Ling, J. E. Post, P. J. Heaney, E. S. Ilton, The relationship between Mn oxidation state and structure in triclinic and hexagonal birnessites. *Chem. Geol.* **479**, 216–227 (2018).
37. B. M. Tebo et al., Biogenic manganese oxides: Properties and mechanisms of formation. *Annu. Rev. Earth Planet. Sci.* **32**, 287–328 (2004).
38. U. F. Lingappa, D. R. Monteverde, J. S. Magyar, J. S. Valentine, W. W. Fischer, How manganese empowered life with dioxygen (and vice versa). *Free Radic. Biol. Med.* **140**, 113–125 (2019).
39. K. J. Parchert, M. N. Spilde, A. Porras-Alfaro, A. M. Nyberg, D. E. Northup, Fungal communities associated with rock varnish in Black Canyon, New Mexico: Casual inhabitants or essential partners? *Geomicrobiol. J.* **29**, 752–766 (2012).
40. J. J. Morgan, Kinetics of reaction between O₂ and Mn(II) species in aqueous solutions. *Geochim. Cosmochim. Acta* **69**, 35–48 (2005).
41. C. R. Myers, K. H. Neelson, Bacterial manganese reduction and growth with manganese oxide as the sole electron acceptor. *Science* **240**, 1319–1321 (1988).
42. T. D. Waite, I. C. Wrigley, R. Szymczak, Photoassisted dissolution of a colloidal manganese oxide in the presence of fulvic acid. *Environ. Sci. Technol.* **22**, 778–785 (1988).
43. F. F. Marafatto et al., Rate and mechanism of the photoreduction of birnessite (MnO₂) nanosheets. *Proc. Natl. Acad. Sci. U.S.A.* **112**, 4600–4605 (2015).
44. W. G. Sunda, S. A. Huntsman, G. R. Harvey, Photoreduction of manganese oxides in seawater and its geochemical and biological implications. *Nature* **301**, 234–236 (1983).
45. N. Lang-Yona et al., Insights into microbial involvement in desert varnish formation retrieved from metagenomic analysis. *Environ. Microbiol. Rep.* **10**, 264–271 (2018).
46. A. Esposito et al., Comparison of rock varnish bacterial communities with surrounding non-varnished rock surfaces: Taxon-specific analysis and morphological description. *Microb. Ecol.* **70**, 741–750 (2015).
47. D. E. Northup et al., Diversity of rock varnish bacterial communities from Black Canyon, New Mexico. *J. Geophys. Res. Atmos.* **115**, G02007 (2010).
48. K. R. Kuhlman, P. Venkat, M. T. La Duc, G. M. Kuhlman, C. P. McKay, Evidence of a microbial community associated with rock varnish at Yungay, Atacama Desert, Chile. *J. Geophys. Res.* **113**, G04022 (2008).
49. C. S. Cockell, A. C. Schuerger, D. Billi, E. I. Friedmann, C. Panitz, Effects of a simulated martian UV flux on the cyanobacterium, *Chroococcidiopsis* sp. 029. *Astrobiology* **5**, 127–140 (2005).
50. D. Billi, E. I. Friedmann, K. G. Hofer, M. G. Caiola, R. Ocampo-Friedmann, Ionizing-radiation resistance in the desiccation-tolerant cyanobacterium *Chroococcidiopsis*. *Appl. Environ. Microbiol.* **66**, 1489–1492 (2000).
51. C. Faglierone et al., Avoidance of protein oxidation correlates with the desiccation and radiation resistance of hot and cold desert strains of the cyanobacterium *Chroococcidiopsis*. *Extremophiles* **21**, 981–991 (2017).
52. D. C. Lacap-Bugler et al., Global diversity of desert hypolithic cyanobacteria. *Front. Microbiol.* **8**, 867 (2017).
53. X. Nguyen, S. Sumimoto, S. Suda, Unexpected high diversity of terrestrial cyanobacteria from the campus of the University of the Ryukyus, Okinawa, Japan. *Microorganisms* **5**, 69 (2017).
54. N. Keren, M. J. Kidd, J. E. Penner-Hahn, H. B. Pakrasi, A light-dependent mechanism for massive accumulation of manganese in the photosynthetic bacterium *Synechocystis* sp. PCC 6803. *Biochemistry* **41**, 15085–15092 (2002).
55. A. Sharma et al., Responses of Mn²⁺ speciation in *Deinococcus radiodurans* and *Escherichia coli* to γ -radiation by advanced paramagnetic resonance methods. *Proc. Natl. Acad. Sci. U.S.A.* **110**, 5945–5950 (2013).
56. M. Tsednee et al., Manganese co-localizes with calcium and phosphorus in *Chlamydomonas* acidocalcisomes and is mobilized in manganese-deficient conditions. *J. Biol. Chem.* **294**, 17626–17641 (2019).
57. K. Barnese, E. B. Gralla, J. S. Valentine, D. E. Cabelli, Biologically relevant mechanism for catalytic superoxide removal by simple manganese compounds. *Proc. Natl. Acad. Sci. U.S.A.* **109**, 6892–6897 (2012).
58. V. C. Culotta, M. J. Daly, Manganese complexes: Diverse metabolic routes to oxidative stress resistance in prokaryotes and yeast. *Antioxid. Redox Signal.* **19**, 933–944 (2013).
59. A. Sharma et al., Across the tree of life, radiation resistance is governed by antioxidant Mn²⁺, gauged by paramagnetic resonance. *Proc. Natl. Acad. Sci. U.S.A.* **114**, E9253–E9260 (2017).
60. M. J. Daly et al., Accumulation of Mn(II) in *Deinococcus radiodurans* facilitates gamma-radiation resistance. *Science* **306**, 1025–1028 (2004).
61. M. J. Daly et al., Small-molecule antioxidant proteome-shields in *Deinococcus radiodurans*. *PLoS One* **5**, e12570 (2010).
62. K. H. Neelson, Ex-phot: A new take on primitive utilization of solar energy. *Environ. Microbiol. Rep.* **7**, 33–35 (2015).
63. F. S. Archibald, I. Fridovich, Manganese and defenses against oxygen toxicity in *Lactobacillus plantarum*. *J. Bacteriol.* **145**, 442–451 (1981).
64. D. S. Macholdt et al., Characterization and differentiation of rock varnish types from different environments by microanalytical techniques. *Chem. Geol.* **459**, 91–118 (2017).
65. J. E. Johnson, S. M. Webb, C. Ma, W. W. Fischer, Manganese mineralogy and diagenesis in the sedimentary rock record. *Geochim. Cosmochim. Acta* **173**, 210–231 (2016).
66. J. E. Johnson et al., Real-time manganese phase dynamics during biological and abiotic manganese oxide reduction. *Environ. Sci. Technol.* **50**, 4248–4258 (2016).
67. S. M. Webb, SIXPack a graphical user interface for XAS analysis using IFFFIT. *Phys. Scr.* **115**, 1011 (2005).
68. S. M. Webb, I. McNulty, C. Eyberger, B. Lai, The MicroAnalysis toolkit: X-ray fluorescence image processing software. *AIP Conf. Proc.* **1365**, 196–199 (2011).
69. E. Bolyen et al., Reproducible, interactive, scalable and extensible microbiome data science using QIIME 2. *Nat. Biotechnol.* **37**, 852–857 (2019).
70. B. J. Callahan et al., DADA2: High-resolution sample inference from Illumina amplicon data. *Nat. Methods* **13**, 581–583 (2016).
71. T. Z. DeSantis et al., Greengenes, a chimera-checked 16S rRNA gene database and workbench compatible with ARB. *Appl. Environ. Microbiol.* **72**, 5069–5072 (2006).

72. J. Oksanen *et al.*, *Vegan: Community Ecology Package* (R package, v. 2.4–6; R Foundation for Statistical Computing, Vienna, 2018).
73. A. Dhariwal *et al.*, *MicrobiomeAnalyst: A web-based tool for comprehensive statistical, visual and meta-analysis of microbiome data*. *Nucleic Acids Res.* **45**, W180–W188 (2017).
74. E. Pruesse, J. Peplies, F. O. Glöckner, SINA: Accurate high-throughput multiple sequence alignment of ribosomal RNA genes. *Bioinformatics* **28**, 1823–1829 (2012).
75. N. Galtier, M. Gouy, C. Gautier, SEAVIEW and PHYLO_WIN: Two graphic tools for sequence alignment and molecular phylogeny. *Comput. Appl. Biosci.* **12**, 543–548 (1996).
76. S. Guindon *et al.*, New algorithms and methods to estimate maximum-likelihood phylogenies: Assessing the performance of PhyML 3.0. *Syst. Biol.* **59**, 307–321 (2010).
77. F. Meyer *et al.*, The metagenomics RAST server—a public resource for the automatic phylogenetic and functional analysis of metagenomes. *BMC Bioinformatics* **9**, 386 (2008).
78. A. P. Arkin *et al.*, KBase: The United States Department of Energy Systems Biology Knowledgebase. *Nat. Biotechnol.* **36**, 566–569 (2018).
79. H. Li, BFC: Correcting Illumina sequencing errors. *Bioinformatics* **31**, 2885–2887 (2015).
80. A. M. Bolger, M. Lohse, B. Usadel, Trimmomatic: A flexible trimmer for Illumina sequence data. *Bioinformatics* **30**, 2114–2120 (2014).
81. B. Bushnell, BBMap: A Fast, Accurate, Splice-Aware Aligner. <https://www.osti.gov/servlets/purl/1241166>. Accessed 10 April 2019.
82. D. Li, C.-M. Liu, R. Luo, K. Sadakane, T.-W. Lam, MEGAHIT: An ultra-fast single-node solution for large and complex metagenomics assembly via succinct de Bruijn graph. *Bioinformatics* **31**, 1674–1676 (2015).
83. S. Nurk, D. Meleshko, A. Korobeynikov, P. A. Pevzner, metaSPAdes: A new versatile metagenomic assembler. *Genome Res.* **27**, 824–834 (2017).
84. Y. Peng, H. C. M. Leung, S. M. Yiu, F. Y. L. Chin, IDBA-UD: A de novo assembler for single-cell and metagenomic sequencing data with highly uneven depth. *Bioinformatics* **28**, 1420–1428 (2012).
85. Y.-W. Wu, B. A. Simmons, S. W. Singer, MaxBin 2.0: An automated binning algorithm to recover genomes from multiple metagenomic datasets. *Bioinformatics* **32**, 605–607 (2016).
86. D. D. Kang, J. Froula, R. Egan, Z. Wang, MetaBAT, an efficient tool for accurately reconstructing single genomes from complex microbial communities. *PeerJ* **3**, e1165 (2015).
87. D. H. Parks *et al.*, Recovery of nearly 8,000 metagenome-assembled genomes substantially expands the tree of life. *Nat. Microbiol.* **2**, 1533–1542 (2017).
88. P.-A. Chaumeil, A. J. Mussig, P. Hugenholtz, D. H. Parks, GTDB-Tk: A toolkit to classify genomes with the genome taxonomy database. *Bioinformatics* **36**, 1925–1927 (2019).
89. T. Brettin *et al.*, RASTtk: A modular and extensible implementation of the RAST algorithm for building custom annotation pipelines and annotating batches of genomes. *Sci. Rep.* **5**, 8365 (2015).
90. T. Aramaki *et al.*, KofamKOALA: KEGG ortholog assignment based on profile HMM and adaptive score threshold. *Bioinformatics* **36**, 2251–2252 (2019).
91. E. D. Graham, J. F. Heidelberg, B. J. Tully, Potential for primary productivity in a globally-distributed bacterial phototroph. *ISME J.* **12**, 1861–1866 (2018).
92. P. G. Bagos, T. D. Liakopoulos, I. C. Spyropoulos, S. J. Hamodrakas, PRED-TMBB: A web server for predicting the topology of beta-barrel outer membrane proteins. *Nucleic Acids Res.* **32**, W400–W404 (2004).
93. R. Carpentier, *Photosynthesis Research Protocols* (Humana Press, 2004).
94. M. M. Werst, C. E. Davoust, B. M. Hoffman, Ligand spin densities in blue copper proteins by q-band proton and nitrogen-14 ENDOR spectroscopy. *J. Am. Chem. Soc.* **113**, 1533–1538 (1991).
95. C. E. Davoust, P. E. Doan, B. M. Hoffman, Q-band pulsed electron spin-echo spectrometer and its application to ENDOR and ESEEM. *J. Magn. Reson. A* **119**, 38–44 (1996).
96. A. Schweiger, G. Jeschke, *Principles of Pulse Electron Paramagnetic Resonance* (Oxford University Press, 2001).
97. B. M. Hoffman, V. J. Deroose, J. L. Ong, C. E. Davoust, Sensitivity enhancement in field-modulated CW ENDOR via RF bandwidth broadening. *J. Magn. Reson. A* **110**, 52–57 (1994).
98. U. Lingappa *et al.*, Metagenome studying the desert varnish. NCBI BioProject. <https://www.ncbi.nlm.nih.gov/bioproject/PRJNA630476/>. Deposited 5 May 2020.
99. U. Lingappa *et al.*, Binned genomes from arnish metagenomes. CaltechDATA. <https://dx.doi.org/10.22002/D1.1960>. Deposited 1 May 2021.